RESEARCH ARTICLE

Rising Stars

ADVANCED
OPTICAL
MATERIALS

www.advopticalmat.de

Increasing the Power: Absorption Bleach, Thermal Quenching, and Auger Quenching of the Red-Emitting Phosphor K_2TiF_6:Mn^{4+}

Jur W. deWit, Thomas P. van Swieten, Marie Anne van deHaar, Andries Meijerink, and Freddy T. Rabouw*

Mn^{4+}-doped fluorides are popular phosphors for warm-white lighting, converting blue light from light-emitting diodes (LEDs) into red light. However, they suffer from droop, that is, decreasing performance at increasing power, limiting their applicability for high-power applications. Previous studies highlight different causes of droop. Here, a unified picture of droop of Mn^{4+}-doped K_2TiF_6, accounting for all previously proposed mechanisms, is provided. Combining continuous-wave and pulsed experiments on samples of different Mn^{4+} content with kinetic Monte Carlo modeling, the contributions of absorption bleach, thermal quenching, and Auger quenching at different excitation densities, are quantified. This work contributes to understanding the fundamental limitations of these materials and may inspire strategies to make Mn^{4+}-doped fluorides more efficient in high-power applications.

1. Introduction

Phosphor-converted white light-emitting diodes (w-LEDs) play a crucial role in many lighting applications. A blue-emitting (In,Ga)N chip and a color-converting phosphor layer together produce white light. Ce^{3+}-doped yttrium aluminum garnet (YAG:Ce^{3+}) is a common phosphor used to convert blue to yellow light.[1,2] A blue LED combined with YAG:Ce^{3+} produces bluish or "cold" white light, while warm white light is often desired for indoor lighting.[3] Currently, warm white light is obtained by the addition of Eu^{2+}-doped $CaAlSiN_3$ (CASN:Eu^{2+}) to the phosphor layer, which introduces a broad-band emission ranging from orange to

infrared.[4] This does not only create a warmer white color but also generally raises the color rendering index, thereby making the color of the lamp more pleasant to the human eye.[5] However, it comes with the downside of decreased luminous efficacy due to emission at wavelengths where the eye is less sensitive.[6]

An alternative class of red-emitting materials with higher luminous efficacy than CASN:Eu^{2+}, is the Mn^{4+}-doped fluorides.[7–9] These materials have absorption bands in the ultraviolet (UV) and blue due to spin-allowed transitions. Their room-temperature wet-chemical synthesis is relatively simple and the narrow emission lines around 630 nm give rise to a red color with a high luminous efficacy.[10,11] These properties make Mn^{4+}-doped fluorides excellent blue-to-red converting phosphors for low-power applications such as displays. However, for lighting applications where the light powers are generally orders of magnitude higher, the use of Mn^{4+}-doped fluorides is complicated by droop: at increasing blue illumination powers, the output of the phosphor increases sub-linearly, approaches a maximum, and may eventually even drop.[12–14] These phenomena can occur already at excitation densities of 100 W cm^{-2} that are typical in (home) lighting w-LEDs and negatively affect the energy efficiency and the perceived color of Mn^{4+}-containing w-LEDs.[15]

The origin of luminescence droop of Mn^{4+}-doped fluorides is not entirely clear and various mechanisms have been proposed. For example, Mn^{4+}-doped fluorides are known to suffer from temperature quenching above temperatures of 400–500 K.[16] Illumination-induced heating may hence lead to an efficiency drop at high excitation powers.[17] In addition, the long 5–10 ms lifetime of the ^2E excited state of Mn^{4+} could contribute to droop as it results in a high steady-state population of excited Mn^{4+} ions. Excited Mn^{4+} ions bleach the $^4A_2 \rightarrow {}^4T_2$ absorption, which ultimately limits the photon conversion rate per Mn^{4+} dopant to an amount equal to the inverse of the lifetime. More indirectly, the high steady-state population of excited Mn^{4+} at high excitation powers may lead to additional losses through excited-state absorption of the blue excitation light or through Auger energy transfer.[18] These losses could be remedied in part by gentle illumination-induced heating up to 400 K because the radiative lifetime and, hence, the steady-state ^2E excited state population decrease with temperature without the loss of light output.[19]

J. W. Wit, T. P. van Swieten, A. Meijerink, F. T. Rabouw
Debye Institute for Nanomaterials Science
Utrecht University
Princetonplein 1, Utrecht 3584 CC, The Netherlands
E-mail: f.t.rabouw@uu.nl
M. A. Haar
Seaborough Research B.V.
Matrix VII Innovation Center
Science Park 106, Amsterdam 1098 XG, The Netherlands

ADVANCED
SCIENCE NEWS

www.advancedsciencenews.com

ADVANCED
OPTICAL
MATERIALS

www.advopticalmat.de

While the various possible saturation and quenching mechanisms have been highlighted separately in previous studies, an overarching understanding of their relative contributions and of the potential avenues to alleviate droop has been missing.

In this paper, we quantify the contributions of thermal quenching, absorption bleach, and Auger quenching to droop of the red-emitting phosphor K_2TiF_6:Mn^{4+}. We perform our experiments and modeling on a set of samples with increasing Mn^{4+} doping concentration. Under blue continuous-wave (CW) illumination at increasing intensity, different samples show droop to a different extent. With a combination of luminescence thermometry based on the intensity ratio between anti-Stokes and Stokes emission lines of Mn^{4+}, reference measurements under pulsed excitation, and kinetic Monte Carlo modeling, we explain the different droop behaviors quantitatively.

2. Results

Figure 1 gives an overview of the temperature-dependent optical properties of K_2TiF_6 (KTF) doped with 0.1 mol% Mn^{4+} with respect to Ti^{4+}. The measurements are done at low excitation power to avoid illumination-induced heating. The emission spectrum upon blue excitation (Figure 1a) shows a set of sharp emission lines due to the transition from ^2E lowest excited state to the $^4A_2$ ground state. By elevating the temperature, the high-energy emission bands increase in intensity compared to the low-energy emission bands. The photoluminescence decay (Figure 1b) is single-exponential in all cases and accelerates for increasing temperatures. The $^2E \rightarrow {}^4A_2$ transition is forbidden by both the spin and the parity selection rule, which explain the long lifetime of 5.8 ms at room temperature. The parity selection rule is relaxed by coupling to three distinct odd-parity vibrations, which are visible as three vibronic lines on either side of the zero-phonon line at 624 nm.

The temperature dependencies of the emission spectra (Figure 1a,c) and excited-state lifetime (Figure 1b,d) are both a consequence of the vibronic nature of the emission. The rate of emission through a vibronic transition is proportional to the phonon occupation $n(T)$ for anti-Stokes emission or to $n(T) + 1$

for Stokes emission. Here, $n(T)$ of a mode with phonon energy $h\nu$ increases with temperature T as

$$n(T) = \frac{1}{e^{h\nu/k_BT} - 1} \tag{1}$$

where k_B is the Boltzmann constant. Indeed, we observe that the anti-Stokes/Stokes intensity ratio increases (Figure 1c) and the excited-state lifetime decreases (Figure 1d) with increasing temperature. The decrease in lifetime between room temperature and 430 K is due to temperature-dependent vibronic coupling, while the sharp drop at 430 K is due to thermal quenching by nonradiative crossover through the $^4T_2$ state.[20]

For our further analysis and modeling, we model the temperature dependencies of the anti-Stokes/Stokes ratio and the excited-state lifetime by approximating the combined contribution of the vibrational modes of energies $h\nu_6 = 216$ cm^{-1}, $h\nu_4 = 325$ cm^{-1}, and $h\nu_3 = 630$ cm^{-1} (see spectrum; Figure 1a) as if it were due to a single phonon mode of effective energy $h\nu_{eff}$. Details of the model and parameters are provided in Section S1, Supporting Information. The experimental anti-Stokes/Stokes ratios show an approximately exponential dependence on the inverse temperature,

$$\frac{I_{AS}}{I_S} = c\, e^{-h\nu_{eff}/k_BT} \tag{2}$$

where $c = 1.14$ is a prefactor that accounts for effects such as differences in the density of optical states at the anti-Stokes and Stokes emission energies, and $h\nu_{eff} = 283$ cm^{-1} (Figure 1c).[21] The excited-state lifetime $\tau(T)$ is determined by a combination of vibronic emission and thermal quenching:[20]

$$\tau(T) = \left[k_{rad}(0) \coth\left(h\nu_{eff}/2k_BT \right) + k_{nonrad}(0)\, e^{-E_{act}/k_BT} \right]^{-1} \tag{3}$$

where $k_{rad}(0)$ and $k_{nonrad}(0)$ are the vibronic emission and nonradiative crossover rates at 0 K, respectively, and E_{act} is the activation energy for crossover.[20] We fit the experimental temperature-dependent lifetimes to Equation (3), yielding
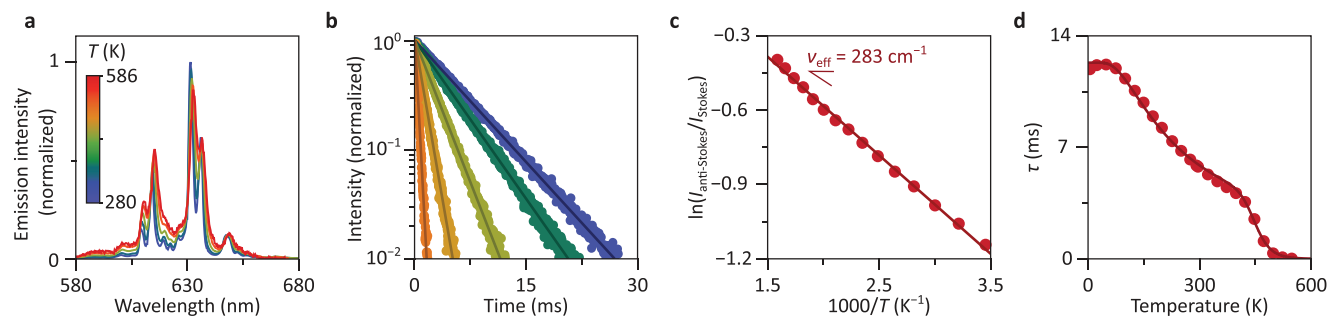

Figure 1. Temperature-dependent optical properties of K_2TiF_6:Mn^{4+}. a) Temperature-dependent emission spectra of KTF:0.1% Mn^{4+} upon 460-nm excitation. With increasing temperature, the relative intensity of anti-Stokes emission bands increases compared to the Stokes emission bands. b) Temperature-dependent photoluminescence decay of the red emission, using the same color coding as in panel (a). Excitation wavelength is 450 nm and detection wavelength is 631 nm. c) Logarithm of the anti-Stokes/Stokes ratio as a function of inverse temperature. Solid line: fit to Equation (2). d) Fitted excited-state lifetime as a function of temperature. Solid line: fit to Equation (3). The errors on the data points in panels (c,d) are estimated to be <0.3% by propagating Poisson counting noise on the spectral measurement to an estimated error in the intensity ratios, and considering the standard error on the lifetime value from a single-exponential fit.
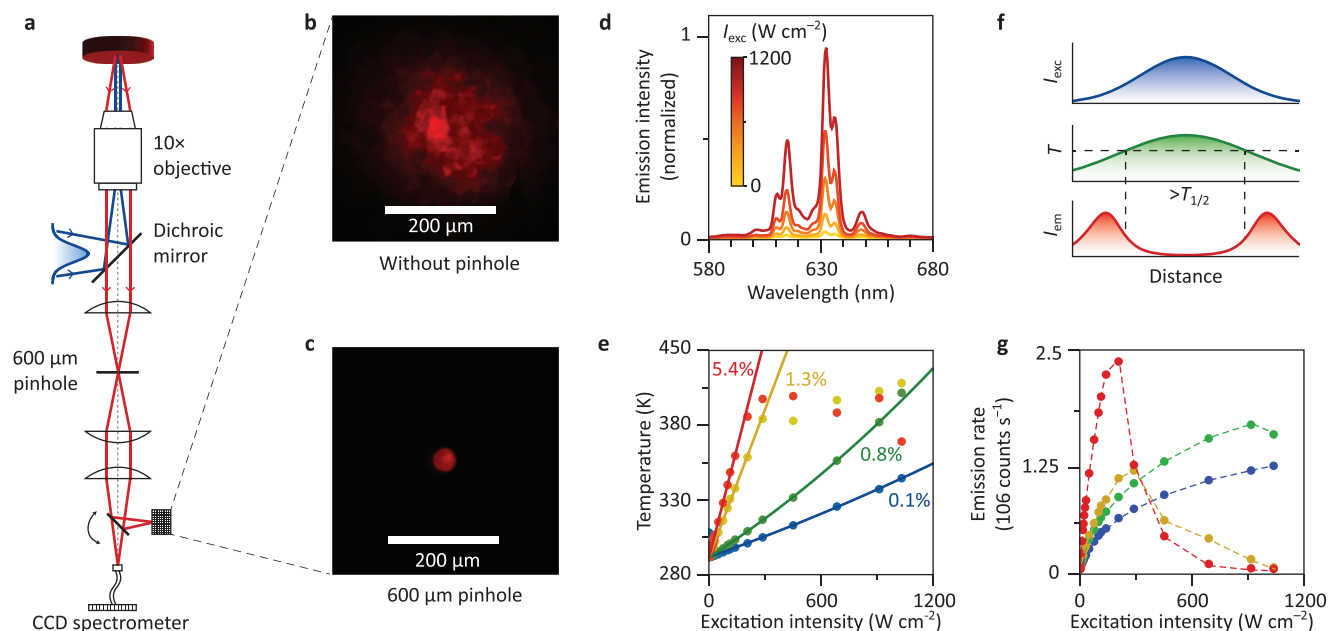
Figure 2. Simultaneous saturation measurements and in-situ thermometry. a) Schematic of the optical setup used for our saturation experiments. The 460-nm excitation light is weakly focused on the back-focal plane of the objective to excite the powder with a spot size of ≈200 µm in diameter. The luminescence image is magnified by a factor 10 onto a pinhole that transmits a part to a spectrometer. b) Image of the phosphor luminescence. c) Same as in panel (b), but with a 600-µm-diameter pinhole in the detection path. d) Emission spectra of the 0.1%-doped sample as a function of excitation intensity I_{exc}. e) Temperature of the 0.1%- (blue), 0.8%- (green), 1.3%- (yellow), and 5.4%-doped sample (red), calculated using the measured anti-Stokes/Stokes ratio and the calibration of Figure 1b, as a function of I_{exc}. Solid lines: empirical second-order polynomial fits that include only datapoints below 390 K. f) Schematic explaining the discrepancy between actual and apparent temperature due to thermal quenching. A Gaussian excitation spot (top) produces an approximately Gaussian temperature profile (middle). Regions where the temperature exceeds the quenching temperature (bottom) are dark. The apparent temperature is therefore weighted toward the colder regions. g) Total emission intensity as a function of I_{exc} for the same doping concentrations as in panel (e). We excluded any influence of material degradation by verifying that changes in emission intensity with I_{exc} were reversible. Dashed lines are drawn through the datapoints as a guide to the eye.

$k_{rad}(0) = 1/(12.3\ ms)$, $k_{nonrad}(0) = 1.5 \times 10^9\ ms^{-1}$, $h\nu_{eff} = 216\ cm^{-1}$, and $E_{act} = 7100\ cm^{-1}$.

We characterize the saturation behavior of our phosphors under CW excitation with blue light using the custom-built set-up shown in **Figure 2**a. The power of the excitation light is controlled with a calibrated motorized attenuator. Then, an objective weakly focuses the blue excitation light to a spot of 167 µm at full-width-half-maximum (fwhm) onto the sample. The same objective collects the luminescence and a dichroic mirror (500 nm) separates the blue excitation from the red emitted light. The luminescence image of the sample is magnified by a factor 10 onto a 600-µm-diameter pinhole that transmits only the luminescence originating from the center of the excitation spot. This ensures that the detected signal originates from an area that experiences an approximately uniform excitation intensity. The luminescence is either imaged on a CCD camera or sent to a fiber-coupled spectrometer (Figure 2b,c). For our measurements below, the reported excitation intensities are the excitation intensities averaged over the area from which signal is detected (Section S2, Supporting Information).

Figure 2d shows the emission spectra of KTF:Mn^{4+} (0.1%) with blue excitation intensity I_{exc} increasing from 0.04 to 1000 W cm^{-2}. Figure S3, Supporting Information shows the corresponding data for doping concentrations of 0.8%, 1.3%, and 5.4%. To rule out material degradation, return measurements from high I_{exc} back to lower I_{exc} were always performed. Our

maximum excitation intensities of $I_{exc} = 1000$ W cm^{-2} are intensities encountered in practical applications such as projectors and automotive headlights. The temperature-dependent emission spectrum makes Mn^{4+}-doped fluoride phosphors uniquely suitable to distinguish the temperature contributions to droop behavior. At each excitation intensity, we convert the anti-Stokes/Stokes emission intensity ratio (I_{aS}/I_S) in the recorded spectrum to a temperature, using our calibration (Figure 1d; Equation (2)) with a small correction for differences in scattering and detection efficiency between samples (Section S4, Supporting Information).[22] The resulting temperatures for the differently doped samples (Figure 2e) reveal gradual illumination-induced heating, likely caused in large part by the Stokes shift. The temperature of the 0.1%- and 0.8%-doped samples increases approximately linearly with excitation intensity at a rate of 6 °C and 9 °C/(100 W cm^{-2}), respectively. The temperature of the 1.3%- and 5.4%-doped sample increases much more rapidly—at a rate of 37 °C and 55 °C/(100 W cm^{-2}) respectively, which is expected, considering the stronger absorption of the blue excitation light. It is noteworthy that the heating rates do not increase linearly with Mn^{4+} concentration, which we attribute to differences in heat transport and excited volume, caused by, for example, powder packing. The observed temperature levels off around 400 K and then do not increase any further. This observation might be counterintuitive, but it is a consequence of thermal quenching (schematically shown in

**ADVANCED
SCIENCE NEWS**

www.advancedsciencenews.com

**ADVANCED
OPTICAL
MATERIALS**

www.advopticalmat.de

Figure 2f). As the center of the illumination spot heats up to the quenching temperature ($T_{1/2}$ = 453 K), it will stop emitting. The dominant signal that we then record, originates from the edges of the illumination spot where the temperature remains just below the quenching temperature. The apparent temperature from luminescence thermometry can thus not exceed the quenching temperature. We assume for our further analysis, that the actual temperature in the center of the spot (in contrast to the apparent temperature) continues to increase for all I_{exc} following the heating rate observed at temperatures lower than 390 K. We use an empirical quadratic model for the heating as a function of I_{exc}, which makes physical sense as non-radiative processes become more dominant at elevated I_{exc}.[23]

In Figure 2g, the emission intensity is plotted as a function of I_{exc} for the different Mn^{4+} doping concentrations. The dependence is approximately linear for I_{exc} < 50 W cm^{-2}, with a steeper slope for the higher doped samples. Saturation, that is, a sublinear increase of emission intensity with I_{exc}, becomes apparent at I_{exc} > 50 W cm^{-2} for both the 0.1 and 0.8%-doped samples. In the 1.3% and 5.4% doped samples, the emission intensity has a maximum between I_{exc} = 208–287 W cm^{-2} and drops for higher I_{exc}. These maxima coincide with the I_{exc} where the temperature reaches 400 K (Figure 2e). If we extrapolate the temperature fits of the 1.5% and 5.4%-doped samples to I_{exc} = 600 W cm^{-2}, the sample temperature would be 517 and 626 K, respectively, where thermal quenching is severe (Figure 1d). Clearly, the drop in emission intensity at high I_{exc} has a significant contribution from thermal quenching.

While the influence of thermal quenching on droop is obvious in Figure 2g, the contributions of other processes are more difficult to distinguish. Absorption bleach and Auger quenching would both result in gradual saturation of the emission intensity as I_{exc} increases. Simultaneously, illumination-induced heating comes with increasing radiative decay rates (Figure 1c,d), reducing the steady-state excited-state population and thereby counteracting droop, as previously realized by Beers et al.[18] Quantitative modeling of the excited-state relaxation pathways, based on saturation measurements, in-situ thermometry, and pulsed experiments, is necessary to disentangle the various potential contributions to droop.

We first analyze the 0.1%-doped sample, where we assume that contributions from Auger quenching are negligible (large distance between Mn^{4+} ions will prevent energy transfer) so that we can quantify the absorption bleach. Under CW excitation, the phosphor reaches a steady-state situation. In the absence of Auger quenching, the steady state excited-state population p_{ss}, that is, the fraction of Mn^{4+} ions in the excited state, is given by[17]

$$p_{ss} = \frac{\sigma_{abs} I_{exc} / \hbar\omega}{\frac{\sigma_{abs} I_{exc}}{\hbar\omega} + k_{decay}(T)} \quad (4)$$

Here, σ_{abs} is the absorption cross-section for photons of energy $\hbar\omega$ and $k_{decay}(T)$ is the temperature-dependent decay rate of the ^2E state. A derivation can be found in Section S5, Supporting Information. The experimental count rate as measured by the CCD spectrometer in the saturation experiments scales as

$$I_{em} = A\, k_{rad}(T)\, p_{ss} \quad (5)$$

where $k_{rad}(T)$ is the temperature-dependent radiative decay rate of the ^2E state and A is a prefactor that accounts for various experimental factors such as the detection efficiency of the set-up, the amount of material investigated, or the doping concentration. We do not consider the role of excited-state absorption as our model does not explicitly account for penetration of the blue excitation light into the phosphor, so excited-state absorption has no influence on the observed count rate. We fit Equation (5) to the experimental saturation curve of the 0.1%-doped sample (blue line, Figure 2g), neglecting Auger quenching by using Equation (4) for the excited-state population. The temperature at each excitation density (Figure 2d) determines $k_{rad}(T)$ and $k_{nonrad}(T)$ following our calibration (Figure 1d). We find $\sigma_{abs} = 3.1 \times 10^{-19}$ cm^2, which is close to literature values found for the $^4A_2 \rightarrow {}^4T_2$ absorption transition in Mn^{4+} (1.5–7.0 × 10^{-19} cm^2)[17,18] and the isoelectronic ion Cr^{3+} (1.7 × 10^{-19} cm^2).[24]

Based on the analysis of the saturation curve of the 0.1%-doped sample, we can calculate the contribution of absorption bleach and the beneficial effect of illumination-induced heating. Dividing out the experimental prefactor A from the saturation curve yields the emission rate per ion as a function of I_{exc} (**Figure 3**a). For reference, we have added the theoretical situation without any droop effects as a dashed line. Further dividing out $k_{rad}(T)$ yields the excited-state population p_{ss} as a function of I_{exc} (Figure 3b). See Section S5, Supporting Information for further explanation on these conversion procedures. The emission rate per ion approaches the radiative decay rate (Figure 3a) and the excited-state population reaches almost 80% at the highest I_{exc} considered here (Figure 3b). The 80% excited-state population corresponds with an 80% absorption bleach. This alone is sufficient to explain the droop (Figure 2g). Illumination-induced heating has a small beneficial effect:[19] the emission rate per ion reaches 163 s^{-1} at I_{exc} = 1200 W cm^{-2}, including heating to 362 K but would be 140 s^{-1} if the temperature were fixed at 293 K. This results in a 81% absorption bleach at I_{exc} = 1200 W cm^{-2}, including heating, compared to 84% absorption bleach without heating (Figure 3b). Note
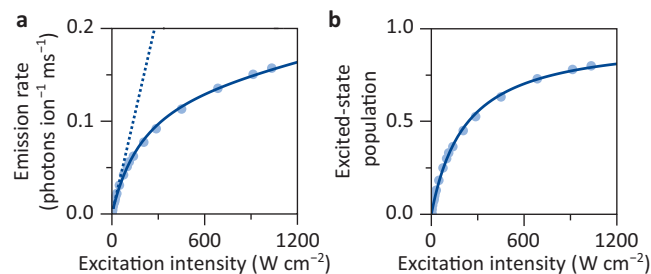

Figure 3. Saturation at low doping concentration. a) Saturation measurement of K_2TiF_6:Mn^{4+}(0.1%) (Figure 2g) converted to the emission rate per ion as a function of excitation intensity I_{exc}. Solid line: fit using the I_{exc}-dependent temperatures from luminescence thermometry experiments in Figure 2e. Dashed line: theoretical emission rate without droop effects. b) Same as in panel (a) but now converted to the excited-state population, that is, the steady-state fraction of Mn^{4+} centers that are in the ^2E excited state.

that our measurements and analysis are blind to excited-state absorption because we measure only luminescence.

The significant excited-state populations at the excitation intensities used in our experiments could cause Auger quenching (**Figure 4**a). Indeed, a recent paper highlighted the issue of Auger quenching in K_2SiF_6:Mn^{4+},[18] a phosphor similar to ours. CW saturation experiments are however not ideal for the quantification of Auger quenching rates because Auger quenching and absorption bleach are difficult to distinguish; both manifest as a gradual decrease of the slope of the saturation curve.

We use ns-pulsed experiments on our highest-doped sample, with 5.4% Mn^{4+} to quantify Auger quenching. The high doping concentration ensures short distances between dopants, making Auger quenching more prominent, while ns-pulsing the excitation laser limits heating and gives a good time resolution to probe excited state dynamics. The photoluminescence decay (Figure 4b) shows an increasingly prominent fast component (at $t < 2$ ms) at increasing excitation fluence. This is indicative of Auger quenching as a higher excitation fluence results in more possibilities for interactions between excited Mn^{4+} ions in close proximity. The time evolution of the anti-Stokes/Stokes ratio reveals negligible laser-induced heating even shortly after the laser pulse and for the highest fluence (Figure 4c). We fit the photoluminescence decay of the highest excitation fluence of $J_{exc} = 2.2$ J cm^{-2} with a kinetic Monte Carlo model. We achieve a good match with the experimental data if we assume dipole–dipole interaction between excited Mn^{4+} ions, with a quenching rate scaling as

$$k_{Auger} = \frac{C_{Auger}}{R^6} \tag{6}$$

where C_{Auger} is the Auger strength and R is the distance between the ions. We assume that an Auger event quenches one of the ions involved, while the other returns to the ^2E emitting state (Figure 4a). The model accounts for the discrete lattice of the KTF crystal. We initiate the model with an excited-state population of $1 - \exp(-\sigma_{abs}J_{exc}/\hbar\omega) = 0.802$ and then track the fate of discrete excited states. Details are given in Section S6, Supporting Information. $C_{Auger} = 657$ nm^6 s^{-1} yields the best fit to the experimental data at $J_{exc} = 2.2$ J cm^{-2} and also provides a good match to the data at lower fluences (Figure 4b). This corresponds to an Auger quenching rate of $k_{Auger} = 64 \times 10^3$ s^{-1} between nearest-neighbor ($R = 4.66$ Å) excited Mn^{4+} ions, more than two orders of magnitude faster than radiative decay.

Now that we have separately studied thermal quenching, absorption bleach, and Auger quenching, we can combine these to model the full droop behavior of our phosphors. We use a kinetic Monte Carlo algorithm to simulate CW excitation. The model uses the excitation rate $k_{exc} = \sigma_{abs}I_{exc}/\hbar\omega$ from the value found for σ_{abs} (Figure 3a), accounts for temperature-dependent radiative and nonradiative decay (Figure 1d) by using the temperatures from in situ luminescence thermometry (e.g., Figure 2d) as input, and includes Auger quenching (Figure 4). The algorithm continues until a steady-state population p_{ss} is reached. The results from a series of simulations at different I_{exc} can be matched to the experimental saturation curves using Equation (5) by optimizing only the prefactor A.

Figure 5a–d compares the results of the Monte Carlo model to the experimental saturation curves. The overall match is good, especially because a single value for σ_{abs} and a single value for C_{Auger} are used to match all four curves. Deviations are apparent around the I_{exc} where thermal quenching sets in. This is likely the result of temperature gradients in the phosphor powder. Indeed, luminescence thermometry provides an in situ average sample temperature but is blind to locations where the temperature exceeds the quenching temperature. Such temperature hotspots would decrease the emission intensity and could be caused by, for example, a phosphor grain with high defect concentration that acts as a source of heat. Future studies may be able to characterize temperature inhomogeneities in phosphor powders in more detail, perhaps by combining intensity-ratio and lifetime thermometry.

Based on our Monte Carlo model, Figure 5e–h shows the contributions of thermal quenching, absorption bleach, and Auger quenching to droop at different Mn^{4+} doping concentrations and as a function of I_{exc}. Absorption bleach leads to transmission (or backscattering) of excitation light and is the dominant droop mechanism in the lowest-doped phosphors. Auger quenching becomes more important at higher doping concentration, which is a consequence of the strong distance dependence of the Auger quenching rate (Equation (6)). The contributions of absorption bleach and Auger quenching are equally strong in the highest-doped sample with 5.4% Mn^{4+}. Losses due to thermal quenching completely dominate the droop behavior in the high-doped samples at high I_{exc}.

Clearly, illumination-induced heating is a key factor to control the droop characteristics of a Mn^{4+}-doped fluoride
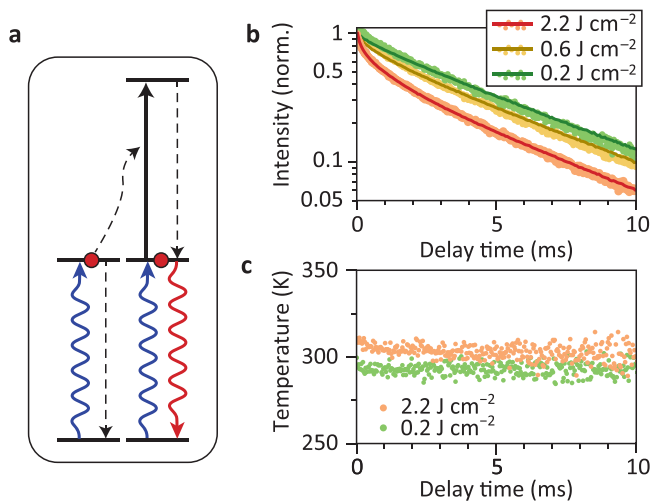

Figure 4. Auger quenching upon ns-pulsed excitation. a) Schematic of Auger quenching by energy-transfer upconversion between Mn^{4+} ions in the ^2E excited state. One excited Mn^{4+} ion transfers its energy to another excited Mn^{4+} ion. The donor ion thereby returns to the $^4A_2$ ground state, while the acceptor ion is raised to the $^4T_1(^4P)$ excited state and quickly relaxes back to the ^2E state. The net effect is the loss of one excited state. b) Photoluminescence decay curves of K_2TiF_6 doped with 5.4% Mn^{4+} excited with 5-ns pulses at high fluences of 0.2 (green), 0.6 (yellow), and 2.2 J cm^{-2} (red). Solid lines: fit to our kinetic Monte Carlo model with $C_{Auger} = 657$ nm^6 s^{-1}. c) Temperature as a function of delay time after pulsed excitation, determined from the time evolution of the ratio of two separate photoluminescence decay measurements of the ν_6 peaks of the anti-Stokes and Stokes emission.
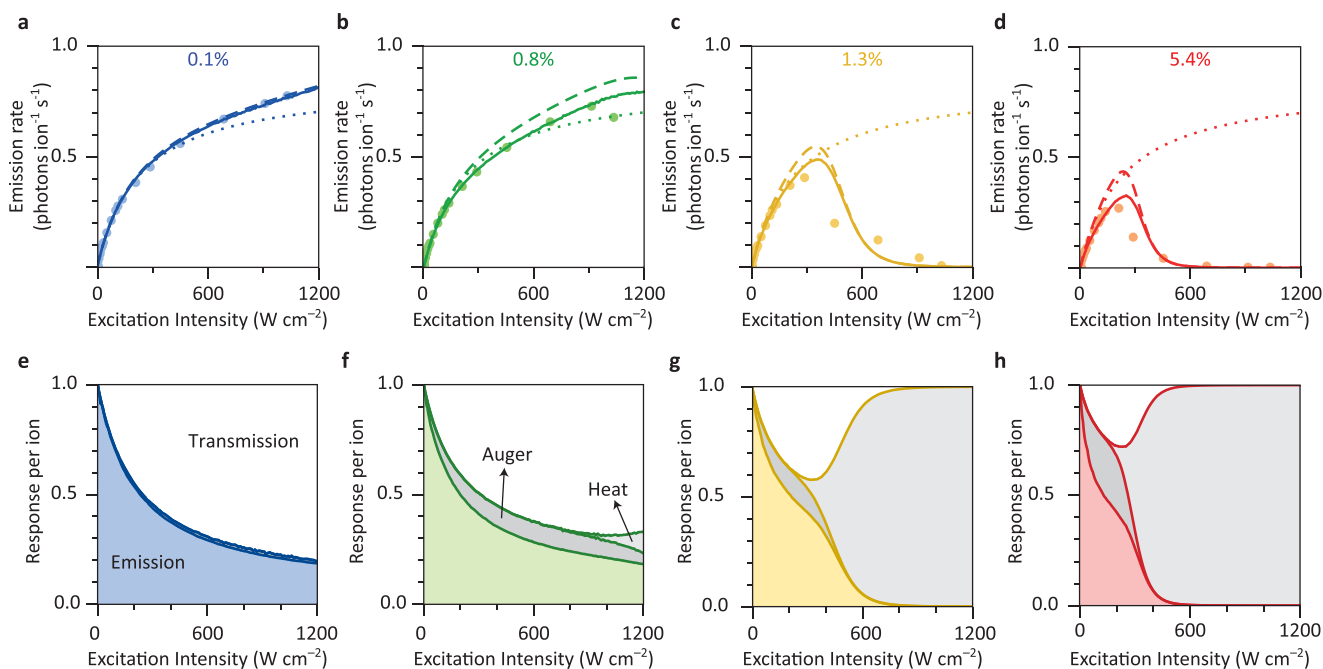
ADVANCED
SCIENCE NEWS
www.advancedsciencenews.com

ADVANCED
OPTICAL
MATERIALS
www.advopticalmat.de

Figure 5. Different contributions to phosphor droop. a–d) Saturation curves of K_2TiF_6 doped with 0.1% Mn^{4+} (a), 0.8% Mn^{4+} (b), 1.3% Mn^{4+} (c), and 5.4% Mn^{4+} (d). Solid lines: fits to our kinetic Monte Carlo model for continuous-wave excitation, using the temperatures measured by luminescence thermometry and parameter values based on the reference measurements of Figures 1,3, and 4. Dotted lines: theoretical emission rate including only the effect of absorption bleach. Dashed lines: emission rate including the effect of heating but without Auger quenching. e–h) Different contributions to phosphor droop as a function of excitation intensity and for the same four samples as in panels (a–d).

phosphor. Mildly elevated temperatures are beneficial for the light output of the phosphor (Figure 3). However, one should prevent that the temperature increases above the thermal quenching threshold. The optimal temperature for the maximum light output is just below the quenching temperature, ≈350–400 K for KTF:Mn^{4+}, where the radiative decay rate is maximum but thermal quenching is negligible. Careful heat management is thus critical when designing devices that hit exactly this optimal phosphor temperature. The absolute light output increases with increasing Mn^{4+} doping concentration (Figure 2g), but the higher doping concentrations are also more sensitive to illumination-induced heating (Figure 2f). These considerations would have to be carefully balanced, depending on the heat management. The tolerance for heating-induced illumination may be increased, allowing for higher phosphor operating temperatures by choosing the right host material of Mn^{4+}. For example, the quenching temperature of K_2SiF_6:Mn^{4+} ($T_{1/2}$ = 558 K) is higher than that of K_2TiF_6:Mn^{4+} ($T_{1/2}$ = 453 K) used in this work.

The present results are highly relevant for the commercial application of Mn^{4+}-doped phosphors for general lighting. Typical doping concentrations for commercial phosphors are 5–10%, required to reach sufficient absorption of blue light. The results in Figure 5 show that at these doping concentrations and typical excitation densities of 100 W cm^{-2} in w-LEDs Auger quenching contributes substantially to droop. It is evident that in lighting applications, the high I_{exc} unavoidably lead to high excited-state populations, determined by the balance between absorption and emission rates (Equation (4)). Auger quenching due to interactions between excited Mn^{4+} ions can be minimized by lowering the doping concentration, as apparent

from Figure 5e–h. This solution may however come at the cost of a larger amount of required phosphor material in a device. Auger quenching could be further reduced by incorporation of Mn^{4+} in a fluoride host where the nearest-neighbor Mn^{4+}–Mn^{4+} distance is large (>10 Å) and radiative decay can outcompete Auger quenching even in nearest neighbor pairs. Alternatively, one could reduce excited-state populations; thus, reducing both Auger quenching and absorption bleach, by increasing the decay rate of the excited state (k_{decay} in Equation (4)). Available tuning knobs are the choice of host material (e.g., k_{decay} = 0.167 ms^{-1} for K_2TiF_6:Mn^{4+} at room temperature versus 0.115 ms^{-1} for K_2SiF_6:Mn^{4+}), temperature management, and finally, (nano)photonic design. (Nano)photonic structures, such as waveguides or antennas, can in principle increase radiative decay rates by orders of magnitude. Fabrication and embedding of the phosphor will however be increasingly challenging and costly for real-live devices and applications.

3. Conclusion

In summary, we have quantified the contributions of absorption bleach, Auger quenching, and thermal quenching to the droop of four different K_2TiF_6 phosphor samples with different Mn^{4+} doping concentrations. All three processes contribute to the droop, to amounts depending on the continuous-wave excitation intensity up to 1200 W cm^{-2} and on the doping concentration. Follow-up work could aim at including scattering and temperature inhomogeneities into the analysis and modeling. In addition, the effect of excited-state absorption on the transmission of blue LED light was beyond the scope of this work

but is important to consider for the performance of a complete device. Our work highlights the unique temperature-dependent optical properties of Mn^{4+}-doped fluorides, which provide opportunities for new LED architectures with improved performance. An interesting engineering challenge would be to operate a Mn^{4+}-based phosphor at the temperature sweet spot where excited-state decay is accelerated but the luminescence is not yet quenched. We show that a combination of Mn^{4+} doping concentration, excitation intensity, and heat regulation could determine the optimal operating conditions. Our results and modeling will contribute to the development of these and other strategies to mitigate droop of Mn^{4+}-based phosphors for high-power warm-white lighting.

4. Experimental Section

Synthesis: The samples synthesized by Senden et al.[20] were used in this investigation. All Mn^{4+}-doping concentrations were experimentally determined with ICP-OES measurements and were given in mol% Mn^{4+} with respect to Ti^{4+}. Further details about the procedure and chemicals can be found there.

Characterization: The procedures of the temperature-dependent optical measurements are described by Senden et al.[20] The steady-state saturation measurements were performed with a Coherent Genesis CX-460 CW laser and an AvaSpec-HSC 1024×58 TEC-EVO CCD spectrometer equipped with an optical fiber. The blue light intensity was modulated with the Standa 10MVAA motorized attenuator and measured with a Thorlabs S405C thermal power sensor. The pulsed Auger quenching experiments were performed with an Ekspla NT342B OPO laser at a repetition rate of 10 Hz and a pulse width of 5 ns as excitation source. Its emission profile was measured with a 1280 × 1024 CMOS camera and the pulse energy was recorded with a Thorlabs ES111C pyroelectric sensor. The emission was recorded with a TRIAX 550 monochromator combined with a H74220-60 PMT. The decay curves were recorded using a PicoQuant TimeHarp 260 computer card.

Supporting Information

Supporting Information is available from the Wiley Online Library or from the author.

Conflict of Interest

The authors declare no conflict of interest.

Data Availability Statement

The data that support the findings of this study are available from the corresponding author upon reasonable request.

[1] T. Takahashi, S. Adachi, *J. Electrochem. Soc.* **2008**, *155*, E183.

[2] S. Nishiura, S. Tanabe, K. Fujioka, Y. Fujimoto, *Opt. Mater.* **2011**, *33*, 688.

[3] M. A. van de Haar, J. Werner, N. Kratz, T. Hilgerink, M. Tachikirt, J. Honold, M. R. Krames, *Appl. Phys. Lett.* **2018**, *112*, 132101.

[4] X. Piao, K. Machida, T. Horikawa, H. Hanzawa, Y. Shimomura, N. Kijima, *Chem. Mater.* **2007**, *19*, 4592.

[5] R. J. Xie, N. Hirosaki, T. Takeda, T. Suehiro, *ECS J. Solid State Sci. Technol.* **2013**, *2*, R3031.

[6] K. Uheda, N. Hirosaki, Y. Yamamoto, A. Naito, T. Nakajima, H. Yamamoto, *Electrochem. Solid-State Lett.* **2006**, *9*, H22.

[7] H. Zhu, C. C. Lin, W. Luo, S. Shu, Z. Liu, Y. Liu, J. Kong, E. Ma, Y. Cao, R.-S. Liu, *Nat. Commun.* **2014**, *5*, 4312.

[8] H. F. Sijbom, R. Verstraete, J. J. Joos, D. Poelman, P. F. Smet, *Opt. Mater. Express* **2017**, *7*, 3332.

[9] D. Chen, Y. Zhou, J. Zhong, *RSC Adv.* **2016**, *6*, 86285.

[10] M. J. Lee, Y. H. Song, Y. L. Song, G. S. Han, H. S. Jung, D. H. Yoon, *Mater. Lett.* **2015**, *141*, 27.

[11] F. Garcia-Santamaria, J. E. Murphy, A. A. Setlur, S. P. Sista, *ECS J. Solid State Sci. Technol.* **2018**, *7*, R3030.

[12] E. Song, Y. Zhou, X.-B. Yang, Z. Liao, W. Zhao, T. Deng, L. Wang, Y. Ma, S. Ye, Q. Zhang, *ACS Photonics* **2017**, *4*, 2556.

[13] M. Kim, W. B. Park, J.-W. Lee, J. Lee, C. H. Kim, S. P. Singh, K.-S. Sohn, *Chem. Mater.* **2018**, *30*, 6936.

[14] Y. Zhou, C. Yu, E. Song, Y. Wang, H. Ming, Z. Xia, Q. Zhang, *Adv. Opt. Mater.* **2020**, *8*, 2000976.

[15] O. B. Shchekin, P. J. Schmidt, F. Jin, N. Lawrence, K. J. Vampola, H. Bechtel, D. R. Chamberlin, R. Mueller-Mach, G. O. Mueller, *Phys. Status Solidi RRL* **2016**, *10*, 310.

[16] W. W. Beers, D. Smith, W. E. Cohen, A. M. Srivastava, *Opt. Mater.* **2018**, *84*, 614.

[17] M. A. Van De Haar, M. Tachikirt, A. C. Berends, M. R. Krames, A. Meijerink, F. T. Rabouw, *ACS Photonics* **2021**, *8*, 1784.

[18] R. A. Osborne, N. J. Cherepy, Z. M. Seeley, S. A. Payne, A. D. Drobshoff, A. M. Srivastava, W. W. Beers, W. W. Cohen, D. L. Schlagel, *Opt. Mater.* **2020**, *107*, 110140.

[19] H. F. Sijbom, J. J. Joos, L. I. D. J. Martin, K. Van den Eeckhout, D. Poelman, P. F. Smet, *ECS J. Solid State Sci. Technol.* **2015**, *5*, R3040.

[20] T. Senden, R. J. A. van Dijk-Moes, A. Meijerink, *Light: Sci. Appl.* **2018**, *7*, 8.

[21] B. Henderson, G. F. Imbusch, *Optical Spectroscopy of Inorganic Solids*, Oxford University Press, Oxford, UK **2006**.

[22] T. P. Van Swieten, T. Van Omme, D. J. Van Den Heuvel, S. J. W. Vonk, R. G. Spruit, F. Meirer, H. P. Garza, B. M. Weckhuysen, A. Meijerink, F. T. Rabouw, *ACS Appl. Nano Mater.* **2021**, *4*, 4208.

[23] C. Hoelen, P. Antonis, D. de Boer, R. Koole, S. Kadijk, Y. Li, V. Vanbroekhoven, P. Van De Voorde, *Proc. SPIE* **2017**, *10378*, 74.

[24] I. Nikolov, X. Mateos, F. Güell, J. Massons, V. Nikolov, P. Peshev, F. Diaz, *Opt. Mater.* **2004**, *25*, 53.